

**IAC-12.C1.6.4****ORBITAL DYNAMICS OF A SOLAR SAIL NEAR L1 AND L2 IN THE ELLIPTIC HILL PROBLEM**

Ariadna Farrés

Math. Institute, Bourgogne Univ. &amp; CNRS, France, ariadna.farres@u-bourgogne.fr

Àngel Jorba

Universitat de Barcelona, Spain, angel@maia.ub.es

**Abstract**

In this paper we study the dynamics of a solar sail close to an asteroid. We have taken the Elliptic Hill problem adding the SRP due to the solar sail as a model. We first describe the dynamics of the system when the eccentricity of the asteroid orbit is neglected. The effect of the solar sail allows us to displace the Lagrangian points  $L_1$  and  $L_2$ . Moreover, we will find families of periodic orbits for different sail orientations. Finally we will show how these invariant objects vary when we include the effect of the eccentricity.

**I. INTRODUCTION**

Due to the small gravitational field around asteroids, solar radiation pressure plays an important role on the dynamics of a satellite around them. Hence, the systematic use of the solar radiation pressure via specialised reflecting areas, such as solar sails, to propel a satellite can offer new and challenging mission concepts.

When looking at the dynamics of a satellite close to an asteroid<sup>8</sup> two effects play an important role: its gravitational field due to its irregular shape and spin states, and the solar attraction and radiation pressure. The first effect becomes relevant when we are within a few radii from the surface of the asteroid, in what is known as the gravity regime. If we are far from the gravity regime, to consider the asteroid as a point mass is a good approximation of the real dynamics. Here effects like the solar radiation pressure and the Sun's gravity must be considered. Moreover, to have a realistic model, the fact that an asteroid can follow a very eccentric orbit around the Sun must also be taken into account.

Solar sails are a proposed form of spacecraft propulsion that takes advantage of the solar radiation pressure (SRP) to propel a spacecraft by means of large and ultra-thin

membrane mirror. The impact of the photons emitted by the Sun on the surface of the sail and its further reflection will accelerate the spacecraft. Although the acceleration produced by the solar radiation pressure is small, given the fact that the asteroids gravitational potential is also small this one will be relevant enough. In fact Villac et al.<sup>9</sup> recently studied the possibility of using the solar arrays of a small satellite as an active control system. They showed that the reflectivity of modest solar panels actually produced an important extra acceleration to the spacecraft.

In this paper we approximate the dynamics of a solar sail close to an asteroid by means of the Elliptic Hill problem with the extra effect of the solar radiation pressure. And we will present a preliminary study the non-linear dynamics around the  $L_1$  and  $L_2$  regions. As an example we will focus on the case of Vesta, and consider a simplified model for the solar sail. This one will be flat and perfectly reflecting. In the near future effects such as the absorption and imperfections on the sail will be taken into account.<sup>7</sup>

In section III. we describe the dynamics of the Circular Hill problem when we add a solar sail. We will describe how the effect of the solar sail displaces the equilibrium points  $L_1$  and  $L_2$  when we consider different sail orien-

tations, having a 2D family of “artificial equilibria”. We will see that the linear dynamics around these points is centre×centre×saddle, hence new families of planar and vertical Lyapunov orbits exist around these artificial equilibria. We will describe how these families vary for different values of the sail orientation.

When we consider the Elliptic Hill problem, we have a periodic time-dependent effect, with the same period as the asteroid orbital period around the Sun ( $T$ ). Now the equilibrium points are replaced by  $T$ -periodic orbits and the periodic orbits are 2D invariant tori. In section IV. we will compute some of these invariant objects and describe how the dynamics changes when we include the effect of the eccentricity.

## II. MODELISATION

One of the options to capture the dynamics of a spacecraft around an asteroid, is to use the Hill problem, that models the motion of two small masses (asteroid and spacecraft) which interact due to their mutual gravitational attraction and are perturbed by a distant larger body (the Sun). In our case the spacecraft is propelled by a solar sail, hence we must add the effect of the solar radiation pressure. This model accounts for the coupled effects of the small body gravity field, the solar tides and the solar radiation pressure.

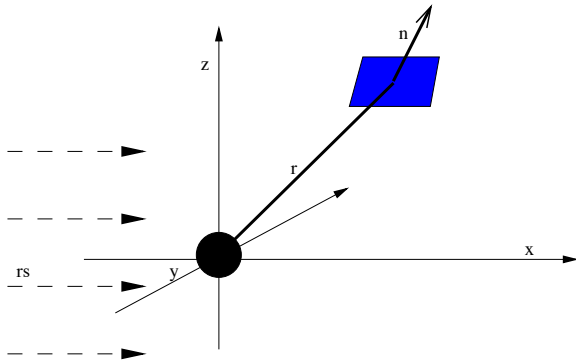


Fig. 1: Schematic representation of the position between the asteroid and the solar sail in the rotating reference system.

### II.I The H3BP for a Solar Sail

The Hill three body problem (H3BP) is obtained as an approximation to the circular restricted three body problem (CR3BP) for a spacecraft orbiting the small primary within the Hill’s radii ( $R_{Hill} = D(\mu_{sb}/3)^{1/3}$ ), where  $\mu_{sb}$  is the

gravitational parameter of the smaller primary (the asteroid) and  $D$  is the distance between the Sun and the small body.

As in the CR3BP, we take a rotating reference frame where the line joining the Sun and the small body is fixed on the  $X$ -axis. But now we take the origin of coordinates centred around the small body and the Sun at  $-\infty$  (see Figure 1).

With this in mind, the equations of motion for the solar sail are:

$$\begin{aligned}\ddot{X} - 2N\dot{Y} &= -\frac{\mu_{sb}}{r^3}X + 3N^2X + a_x, \\ \ddot{Y} + 2N\dot{X} &= -\frac{\mu_{sb}}{r^3}Y + a_y, \\ \ddot{Z} &= -\frac{\mu_{sb}}{r^3}Z - N^2Z + a_z,\end{aligned}\quad (1)$$

where,  $(X, Y, Z)$  denotes the position of the solar sail in the rotating frame,  $N = \sqrt{\mu_{sun}/a_{ast}}$  is the angular velocity of the rotating frame,  $\mu_{sb}$  is the gravitational parameter of the small body,  $r = \sqrt{X^2 + Y^2 + Z^2}$  is the distance between the solar sail and the centre of the small-body, while  $\mathbf{a} = (a_x, a_y, a_z)$  is the acceleration given by the solar sail.

### II.II The EH3BP for a Solar Sail

For a more realistic model, the fact that most asteroids follow very eccentric orbits around the Sun must be taken into account. The Elliptic Hill three body problem (EH3BP) is an extension of the H3BP, which assumes that the small body revolves around the distant perturbing body (the Sun) in an elliptic Keplerian orbit rather than a circular one.

Again, we can find the EH3BP as an approximation of the Elliptic restricted three body problem (ER3BP) for a spacecraft orbiting the small primary within the Hill’s radii. We recall that the ER3BP uses a rotating-pulsating reference system, so that the distance between the primaries remains fixed. Where the new coordinates  $(x, y, z)$  are related to the old ones  $(X, Y, Z)$  by  $X = \rho x, Y = \rho y, Z = \rho z$ , and  $\rho = \frac{1}{1+e \cos f}$ , being  $e$  the eccentricity of the elliptic motion of the asteroid around the Sun and  $f$  the true anomaly. In this new set of coordinates the time variable will be defined by the true anomaly. Finally to derive the EH3BP we will consider the centre the origin of coordinates around the small body and send the Sun to  $-\infty$ .

Now the equations of motion for the solar sail are:

$$\begin{aligned}x'' - 2Ny' &= \frac{1}{1+e \cos f} \left( -\frac{\mu_{sb}}{r^3}x + 3N^2x + a_x \right), \\ y'' + 2Nx' &= \frac{1}{1+e \cos f} \left( -\frac{\mu_{sb}}{r^3}y + a_y \right), \\ z'' + N^2z &= \frac{1}{1+e \cos f} \left( -\frac{\mu_{sb}}{r^3}z + a_z \right),\end{aligned}\quad (2)$$

where  $'$  denotes differentiation with respect to the true anomaly  $f$ ,  $(x, y, z)$  denotes the position of the solar sail in the rotating frame and  $r = \sqrt{x^2 + y^2 + z^2}$  is the distance between the solar sail and the centre of the small-body, while  $N$  and  $\mathbf{a} = (a_x, a_y, a_z)$  are defined as in Eq. (1).

Notice that if we consider  $e = 0$ , Eqs. (2) and (1) turn to be the same, i.e. the H3BP is a particular case of the E3BP.

### II.III Solar Sail

In this paper we will consider the simplest model for a solar sail: the sail is assumed to be flat and perfectly reflecting. Hence the acceleration due to the SRP is in the normal direction to the surface of the sail, and

$$\mathbf{a} = (a_x, a_y, a_z) = \beta \langle \mathbf{l}, \mathbf{n} \rangle^2 \mathbf{n}, \quad (3)$$

where  $\mathbf{l}$  denotes the direction of the SRP,  $\mathbf{n}$  is the vector normal to the surface of the sail (both are unit vectors), and  $\beta$  is the characteristic acceleration of the sail.

In the rotating reference frame considered here  $\mathbf{l} = (1, 0, 0)$  and  $\mathbf{n} = (\cos \alpha \cos \delta, \sin \alpha \cos \delta, \sin \delta)$ , where  $\alpha$  is the angle between  $\mathbf{n}$  and the Sun-line on the ecliptic plane and  $\delta$  is the angle with the  $z$ -axis. As the direction of the SRP cannot point towards the Sun, then  $\langle \mathbf{l}, \mathbf{n} \rangle \geq 0$ .

The characteristic acceleration of a solar sail  $\beta$  is given by,

$$\beta = \frac{\mu_{SRP}}{R^2}; \quad \mu_{SRP} = G_{SRP} \frac{A}{m} (1 + \rho), \quad (4)$$

where  $G_{SRP}$  represents the solar flux,  $\sigma = \frac{A}{m}$  is the area to mass ratio of the spacecraft,  $R$  is the distance between the spacecraft and Sun and  $\rho$  is a coefficient representing the reflectivity of the solar sail, which we take equal to 1 as we are considering the case of a perfectly reflecting sail.

As an example we will consider the case of a modest solar sail, where the area to mass ratio of  $0.025 m^2/kg$ , 100 times smaller than the Nano-Sail D1 mission where they successfully deployed a  $10 m^2$  solar sail with a  $4 kg$  payload. The area to mass ratio considered here accounts for a smaller sail or a larger payload mass for the spacecraft, given by the extra onboard instrumentation.

Given an area to mass ratio of  $0.025 m^2/kg$ , a solar sail in the vicinity of Vesta ( $R \approx 2.3 AU$ ) would have a characteristic acceleration of  $\beta \approx 4.22 \times 10^{-11} km/s^2$ .

### II.IV Parameters

In this paper we consider the particular case of a solar sail orbiting around Vesta. In Table 1 we summarise the values for all the parameters used.

Parameter	Value	Unit
$\mu_{sb}$	17.8	$\frac{km^3}{s^2}$
$\mu_{sun}$	$1.327 \times 10^{11}$	$\frac{km^3}{s^2}$
$a_{ast}$	2.3619	AU
$N$	$5.7086 \times 10^{-8}$	$\frac{1}{s}$
Area/mass ratio	0.025	$\frac{m^2}{kg}$
$G_{SRP}$	$10^8$	$\frac{km^3}{s} \frac{kg}{m^2}$
$e$	0.0882	

Table 1: SRP and Spacecraft Parameters for a mission to Vesta

Finally, we will normalise the units of distance ( $L$ ) and time ( $T$ ) so that they satisfy:  $NT = 1$  and  $\mu_{sb} \frac{T^2}{L^3} = 1$ . In this unit system, the normalised variables  $\bar{x}, \bar{y}, \bar{z}$  and  $\bar{t}$  are related to the unnormalised variables  $x, y, z$ , and  $t$  by:

$$t = \bar{t}T, \quad x = \bar{x}L, \quad y = \bar{y}L, \quad z = \bar{z}L,$$

$$\dot{x} = \dot{\bar{x}}L/T, \quad \dot{y} = \dot{\bar{y}}L/T, \quad \dot{z} = \dot{\bar{z}}L/T,$$

With this normalisations, the equations of motion in Eq. (1) and (2) use  $N = 1$ ,  $\mu_{sb} = 1$  and  $\beta$  is replaced by,

$$\bar{\beta} = \beta \left( \frac{1}{\mu_{sb} N^4} \right)^{1/3}.$$

Where for the case of Vesta we have  $\bar{\beta} = 47.99$ .

### III. DYNAMICS FOR THE H3BPS ( $e = 0$ )

It is well known that the classical Hill problem (no SRP) has two symmetric equilibrium points  $L_{1,2} = (\pm 3^{-1/3}, 0, 0)$ , whose linear dynamics is centre  $\times$  centre  $\times$  saddle. As the system is Hamiltonian, around  $L_{1,2}$  we find families of planar and vertical Lyapunov orbits and Halo orbits. In this section we will discuss how the phase space dynamics varies when we add the effect of the SRP due to a solar sail.

### III.I Artificial Equilibria

It is well known that when we include the effect of SRP in the Hill's problem  $L_{1,2}$  are displaced. Having a 2D family of "artificial" equilibria parametrised by the sail orientation  $\alpha$  and  $\delta$ .

When we consider a solar sail perpendicular to the SRP direction<sup>4</sup> (i.e.  $\alpha = \delta = 0$ ) the Lagrangian points  $L_1$  and  $L_2$  are displaced towards the Sun and lay in the  $x$ -axis, which we will call  $SL_1$  and  $SL_2$  respectively. As we can see in Figure 2,  $SL_1$  quickly moves away from the small body while  $SL_2$  comes close to it. Notice that for  $\bar{\beta} = 47.99$ ,  $SL_1$  is about 16UD from the small body and presenting little interest for mission applications. On the contrary,  $SL_2$  come close to the small-body, and presents a more interesting location. For  $\bar{\beta} = 47.99$   $SL_2$  is at about 0.14UD  $\approx 113$  Vesta's radii. A distance at which the perturbations given by the shape and spin-rate of the asteroids is still not relevant enough and the H3BP for a solar sail is a good approximation for the dynamics around  $SL_2$ .

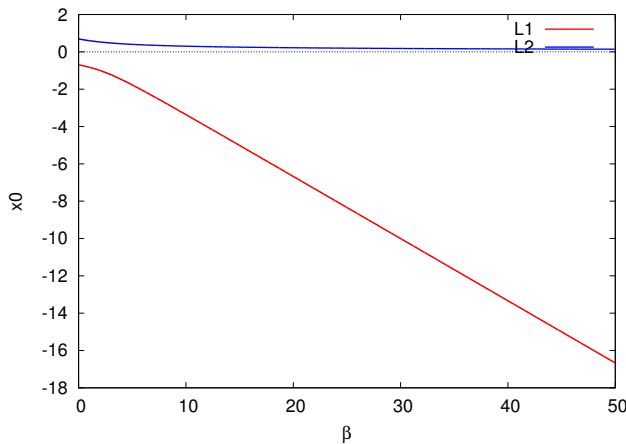


Fig. 2: Normalised distance  $x$  between the displaced  $SL_{1,2}$  and the small-body vs solar acceleration  $\bar{\beta}$ .

We know that the linear dynamics around  $L_{1,2}$  is centre  $\times$  centre  $\times$  saddle and for  $\bar{\beta} \in [0, 50]$   $SL_{1,2}$  inherits the same linear behaviour. To fix notation let  $\pm\lambda_1, \pm i\omega_1, \pm i\omega_2$  be the eigenvalues of the differential flow at the equilibrium point. In Figure 3 we plot the variation of the modulus on the eigenvalues with respect to  $\bar{\beta}$ . Notice that as  $\bar{\beta}$  increases also does the instability of  $SL_2$  (blue line). This is probably because as we get closer to the small body its gravitational effect is stronger. Moreover, the modulus of the complex eigenvalues also increase, this has a direct effect on the period of the family of orbits that are born around the equilibrium point, which will have shorter orbital periods. On the other hand, the in-

stability of the  $SL_1$  decreases,  $\lambda \rightarrow 0$ , as well as the orbital period of the orbits that tends to synchronise itself with the asteroids period.

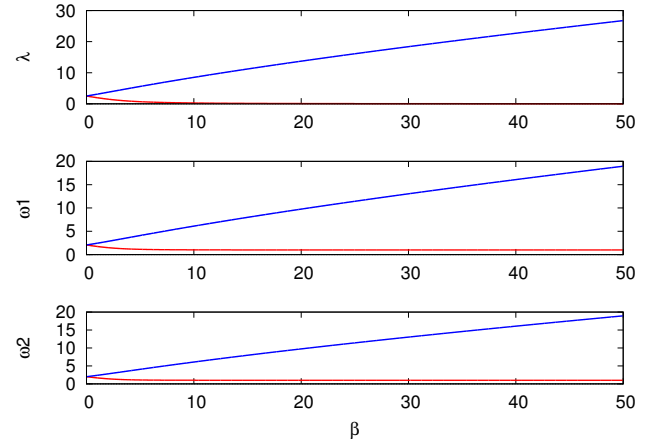


Fig. 3: Modulus of the eigenvalues of the linearised system at the displaced  $SL_{1,2}$  vs  $\bar{\beta}$ . From top to bottom:  $\lambda_1$ ,  $\omega_1$  and  $\omega_2$

When we consider other sail orientations  $\alpha$  and  $\delta \neq 0$  we can displace the equilibria away from the  $x$ -axis. We note that, if we consider  $\alpha \neq 0$  and  $\delta = 0$ , we displace the equilibrium points within the ecliptic plane, from one side to the other w.r.t the  $x$ -axis. While, if we consider  $\alpha = 0$  and  $\delta \neq 0$ , then we displace the equilibrium points above and below the ecliptic plane. The use of these "artificial" equilibria for mission operations at asteroids was already investigated by Morrow et al.<sup>6</sup>

We can find all these equilibrium points with a simple continuation method starting from the classical  $L_1$  or  $L_2$  and varying any of the two angles  $\alpha$  or  $\delta$ . In Figure 4 we show the position of some of these artificial equilibrium points for  $\alpha = 0$ ,  $\delta \in [-\pi/2, \pi/2]$  and  $\bar{\beta} = 5, 10, 20, 30, 40, 50$  (red lines). In blue we represent the family of equilibria for  $\bar{\beta} = 47.99$ . All these points lie on the  $x, z$  plane.

Most of these equilibrium points inherit the dynamics of  $L_1$  and  $L_2$ . Hence, they are unstable and the linear dynamics is centre  $\times$  centre  $\times$  saddle.

### III.II Periodic Orbits

Given the fact that  $SL_1$  quickly escapes from a small vicinity of the asteroid when  $\bar{\beta}$  grows, from now on we will focus on the dynamics close to  $SL_2$ . Here we will describe the families of periodic orbits that appear around the different artificial equilibria.

We just mentioned that the equilibrium points are

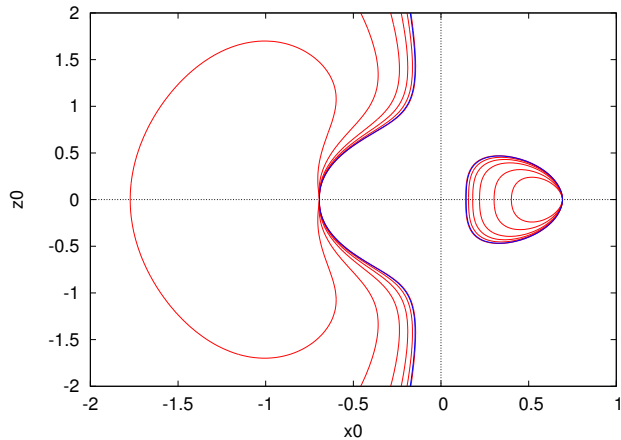


Fig. 4: Position of the fixed points in the  $x$ - $z$  plane for  $\alpha = 0$ ,  $\delta \in [-\pi/2 : \pi/2]$  and  $\beta = 5, 10, 20, 30, 40, 47.99$  and  $50$ .

centre $\times$ centre $\times$ saddle. Moreover, the system is Hamiltonian. Hence, the Lyapunov Centre Theorem<sup>5</sup> ensures that, under a generic non-resonant condition, two families of periodic orbits are born around each equilibrium point. Each family is related to one of the two complex eigenvalue, where the period of the orbits tends to  $2\pi/\omega_i$  as these ones tend to the equilibrium point. Here we describe the families of periodic orbits for  $\bar{\beta} = 47.99$  but a similar behaviour is expected for other values of  $\bar{\beta}$ .

Due to the symmetries of the system both families of orbits cross transversally the Poincaré section  $\Gamma = \{Y = 0, \dot{Y} > 0\}$ . We have computed these two families of periodic orbits by means of a continuation method, taking the  $x$  coordinate of the orbit in the Poincaré section  $\Gamma$  as the continuation parameter.

In Figure 5 we plot the continuation diagram of the planar and vertical family for  $\alpha = \delta = 0$  (i.e. the sail is perpendicular to the SRP). We can see that when the planar family of periodic orbits cross the 1:1 resonance the two families of Halo orbits are born. We note that as the two centre librations of  $SL_2$  are close to a 1:1 resonance ( $i\omega_1 = i18.3921913, i\omega_2 = i18.3831392$ ) the Halo orbit are born very close to  $SL_2$ .

Both the planar and vertical family of periodic orbits that are born at  $SL_2$  are linearly unstable and their linear dynamics is centre $\times$ saddle. At the 1:1 resonance, the linear dynamics of the planar orbit changes, the orbits are still unstable but the linear dynamics is now saddle $\times$ saddle. Moreover, the Halo orbits that are born inherit their dynamics, that is to say they are centre $\times$ saddle orbits. In Figure 5 the dynamics around the orbit is represented by the colour,

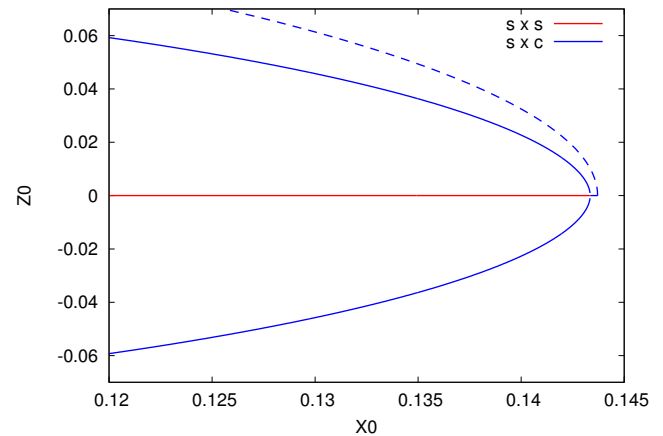


Fig. 5: Continuation diagram of the planar (continuous line) and vertical (dashed line) family of periodic orbits. The orbits in red are saddle $\times$ saddle and the orbits in blue are centre $\times$ saddle

the blue points correspond to centre $\times$ saddle orbits, while the red points correspond to saddle $\times$ saddle orbits.

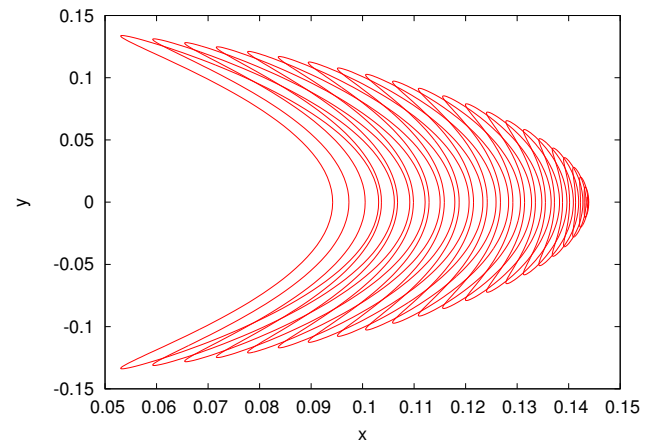


Fig. 6: Planar family of periodic orbits for  $\bar{\beta} = 47.99$ ,  $\alpha = \delta = 0$  and  $e = 0$ .

In Figures 6 and 7 we plot, respectively, some of the orbits in the planar and vertical Lyapunov family around  $SL_2$ . And in Figure 8 we plot their associated Halo orbits.

When we consider  $\alpha = 0, \delta \neq 0$  the picture is slightly different, but the general structure of periodic orbits is the same. Families of planar and Halo orbits still exist, but they are related in a different way. The planar family of periodic orbits that are born from the fixed point are slightly inclined and gain inclination very quickly, having Halo-type orbits. The other branch of Halo-type orbits are related to the planar family and we can go from one to the other by continuation.

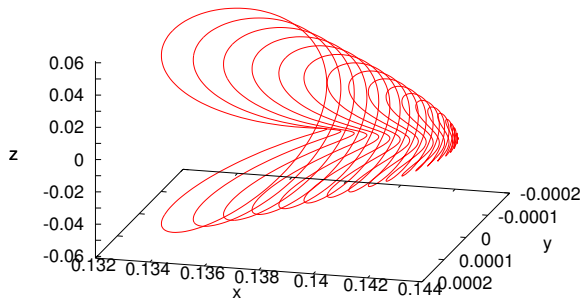


Fig. 7: Vertical family of periodic orbits for  $\bar{\beta} = 47.99$ ,  $\alpha = \delta = 0$  and  $e = 0$ .

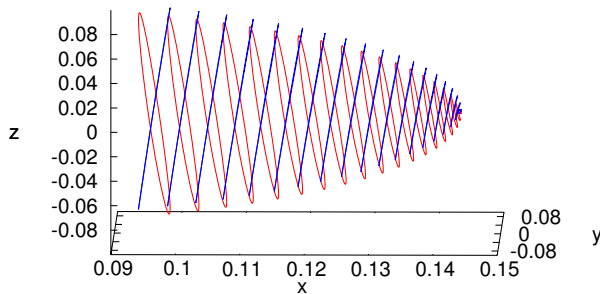


Fig. 8: Upper and lower families of periodic Halo orbits for  $\bar{\beta} = 47.99$ ,  $\alpha = \delta = 0$  and  $e = 0$ .

In Figure 9 we show the continuation diagram for  $\alpha = 0$  and  $\delta = 0, 0.01, 0.02$  and  $0.03$  rad. On the top of Figure 10 we show the families of planar and Halo-type orbits for  $\delta = 0$  and on the bottom of this Figure we see the same family of orbits for  $\delta = 0.02$  rad. Here we can see that the global structure of the system is the same, in both cases we have both planar and Halo type orbits.

In Figure 11 we plot the family of vertical orbits around the fixed point for  $\alpha = 0, \delta = 0.01$ . Notice that we still find orbits with an eight-shape, although now it has no longer two symmetric loops as it happened when  $\delta = 0$  (see Figure 7). On the other hand we must mention that the orbits in the vertical family that are close to the equilibrium point do not have an eight-shape but rather a more circular one. At some point the orbits start bending and end up having an eight-shape.

#### IV. DYNAMICS OF THE EH3BPS ( $e \neq 0$ )

When  $e \neq 0$ , the model becomes a periodic time-dependent differential equation. In this section we will first discuss the main effects of this perturbation on the invari-

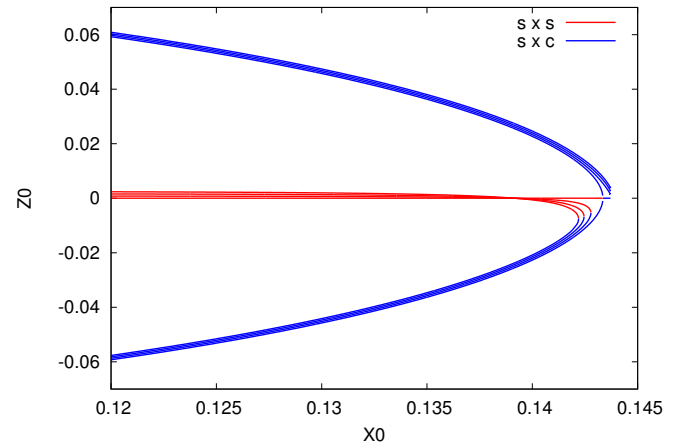


Fig. 9: Continuation diagram for the orbits in the planar family for  $\delta = 0, 0.01, 0.02$  and  $0.03$ . The orbits in red are saddle  $\times$  saddle and the orbits in blue are centre  $\times$  saddle.

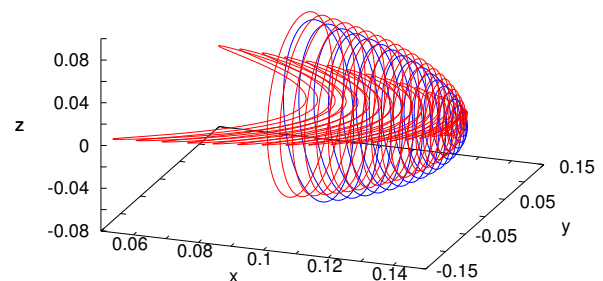
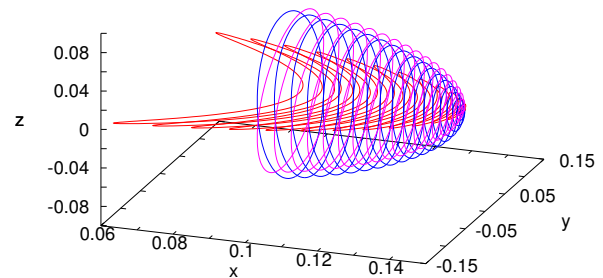


Fig. 10: Planar family of periodic orbits for  $\bar{\beta} = 47.99$ ,  $\alpha = 0$  and  $\delta = 0$  (top) or  $\delta = 0.03$  (bottom) and  $e = 0$ .

ant structures of the phase space of the autonomous model, and then we will use numerical tools to obtain some relevant trajectories.

A first change is that, due to the time-dependence, the points  $SL_{1,2}$  are no longer equilibrium points. It is well known that, under very generic conditions, they are replaced by periodic orbits with the same period as the perturbation ( $2\pi$  in our situation). These periodic orbits tend to the equilibrium points of the unperturbed system when

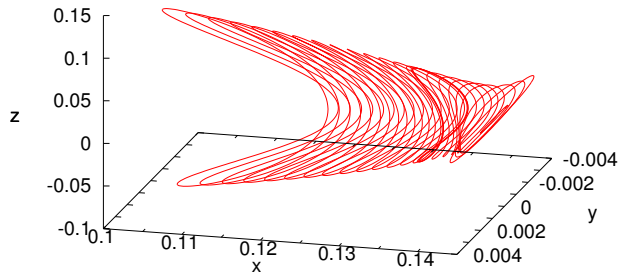


Fig. 11: Vertical family of periodic orbits for  $\bar{\beta} = 47.99$ ,  $\alpha = 0$ ,  $\delta = 0.01$  and  $e = 0$ .

the eccentricity tends to zero.

As in the previous sections, let us now focus on the neighbourhood of  $SL_2$ . As it has been mentioned above, for  $e = 0$  the linear dynamics around  $SL_2$  is of the type centre  $\times$  centre  $\times$  saddle and, for each centre direction, there is a family of periodic orbits departing from the point. These are the so-called Lyapunov families of periodic orbits.

For small values of the eccentricity  $e$ , the  $SL_2$  point is replaced by a periodic orbit of the type centre  $\times$  centre  $\times$  saddle. For each centre direction, there is a one-parametric family of quasi-periodic solutions (2D tori) that replaces the Lyapunov family of periodic orbits of the unperturbed case  $e = 0$ . We will refer to these orbits as Lyapunov families of quasi-periodic solutions. These orbits have two basic frequencies, the perturbing frequency ( $2\pi$ ) and a frequency coming from one of the periodic Lyapunov orbits of the case  $e = 0$ .

The main difference between the quasi-periodic and the periodic Lyapunov families is that, while the periodic families are continuous (i.e., the periodic orbits fill a smooth 2D manifold), the quasi-periodic families are not: the quasi-periodic orbits with resonant frequencies are destroyed, and only the ones with good (Diophantine) frequencies are preserved.<sup>3</sup> This gives a Cantorian structure to the set of Lyapunov orbits, where the holes that produce the Cantor structure are due to resonances between the frequencies of the orbits.

#### IV.I Computation of quasi-periodic orbits

Consider the following (stroboscopic) map: for each initial condition  $p$  for  $f = 0$ , we call  $F(p)$  to the position of the corresponding orbit for  $f = 2\pi$ . A fixed point of  $F$  corresponds to a  $2\pi$  periodic orbit of the flow. In the same way,

a quasi-periodic orbit (with two basic frequencies) of the flow corresponds to an invariant curve of  $F$ . An invariant curve can be represented (parametrized) by a map  $\varphi$  from  $\mathbb{T}^1$  to  $\mathbb{R}^6$  such that

$$F(\varphi(\theta)) = \varphi(\theta + \omega), \quad \text{for all } \theta \in \mathbb{T}^1. \quad (5)$$

Here  $\omega$  denotes the frequency of the curve.

To start the discussion, let us assume that we know the rotation number of the curve we are looking for, and that we want to determine the function  $\varphi$ . So, let us write  $\varphi$  as a real Fourier series,

$$\varphi(\theta) = a_0 + \sum_{k>0} a_k \cos(k\theta) + b_k \sin(k\theta), \quad a_k, b_k \in \mathbb{R}^6.$$

As it is usual in numerical methods, we look for a truncation of this series. So, let us fix in advance a truncation value  $N$  (the selection of the truncation value will be discussed later on), and let us try to determine (an approximation to) the  $2N + 1$  unknown coefficients  $a_0, a_k$  and  $b_k$ ,  $0 < k \leq N$ .

First, let us define a mesh of  $2N + 1$  points on  $\mathbb{T}^1$  (in all the paper we assume that the length of  $\mathbb{T}^1$  is  $2\pi$ ),

$$\theta_j = \frac{2\pi j}{2N + 1}, \quad 0 \leq j \leq 2N.$$

Imposing condition (5) on the points of this mesh we obtain the system of  $2N + 1$  equations,

$$F(\varphi(\theta_j)) - \varphi(\theta_j + \omega) = 0, \quad 0 \leq j \leq 2N, \quad (6)$$

that we will try to solve, by means of the Newton method, to determine the  $2N + 1$  unknown Fourier coefficients.

Hence, we consider a function  $G$  defined as follows: to each array of  $2N + 1$  (Fourier) coefficients  $(a_0, a_1, b_1, a_2, b_2, \dots, a_N, b_N)$ , we associate the  $2N + 1$  values that appear in the left-hand side of (6). Note that, as each coefficient  $a_k$  (or  $b_k$ ) is, in fact, an element of  $\mathbb{R}^6$ , the function  $F$  maps points of  $\mathbb{R}^m$  into  $\mathbb{R}^m$ , where  $m = 6(2N + 1)$ .

Each Newton iteration requires the numerical evaluation of the function  $G$  at a given point as well as its derivatives. The evaluation of  $G$  can be easily done as follows: for a given array of Fourier coefficients it is immediate to compute, by direct evaluation of the Fourier series, the points  $\varphi(\theta_j)$  and the corresponding images by  $F$ ,  $F(\varphi(\theta_j))$ . Finally, the values  $\varphi(\theta_j + \omega)$  are also obtained by direct evaluation of the series. The computation of the Jacobian matrix follows from the chain rule.<sup>1</sup>

Note that, if  $\varphi$  is a Fourier series corresponding to an invariant curve then, for any  $\theta_0 \in \mathbb{T}^1$ ,  $\phi(\theta) \equiv \varphi(\theta + \theta_0)$  is a different Fourier series (i.e., the Fourier coefficients are different) that represents the same invariant curve  $\varphi$ . This implies that the differential of the function  $G$  around an invariant curve will have a one-dimensional kernel. This introduces numerical difficulties when solving the linear system that appears in the Newton method.

To solve this problem we can simply add, for instance, an extra condition imposing that a component of  $\varphi(\theta)$  has a prescribed value when  $\theta$  is zero (of course, there are different options). On one hand, this removes the lack of uniqueness problem and, on the other hand, this can be imposed in a very easy way: we simply add this condition as an extra equation and, as this is a linear condition, we simply add the corresponding row in the Jacobian of  $G$ .

Note that now we have to solve a linear system that has a unique solution, but it is not “squared”: it has an “extra” equation. If, for instance, we are solving the linear system by means of a standard Gaussian elimination method with row pivoting, then the pivoting strategy will take care of sending to the last row the equation that is linearly dependent of the other equations. So, after the triangularisation process and except by rounding errors, the last equation should read like “ $0 = 0$ ”. Hence, we can simply skip this equation and solve the triangular system in the usual way.

#### IV.II Error estimation

Assume that we have found an approximate zero of the function  $G$ . For instance, assume that, for a given frequency  $\omega$ , we have obtained Fourier coefficients such that (6) is satisfied with a tolerance of, say,  $10^{-12}$ . As we do not have any estimation of the discretization error (this error depends on the truncation value  $N$ ), we do not have information on the error of the computed invariant curve. In fact, it could be even possible that what we have computed is not an invariant curve but simply a curve containing a few invariant points.

To deal with these inconveniences, let us consider the value

$$E(\varphi, \omega) = \max_{\theta \in \mathbb{T}^1} |F(\varphi(\theta)) - \varphi(\theta + \omega)|,$$

as an estimate of the error of the invariant curve. It is clear that  $\varphi$  is an invariant curve with rotation number  $\omega$  if and only if  $E(\varphi, \omega)$  is zero.

For each curve, we have approximated the value  $E(x, \omega)$  by simply tabulating its value on a mesh of points on  $\mathbb{T}^1$ . Of course, this mesh must be finer (typically, we have used

a 100 times finer mesh) than the one used to obtain (6) from (5). When this estimate is bigger than a prescribed threshold, the program automatically increases the number of Fourier coefficients and the number of discretizing points (i.e., it increases the truncation value  $N$ ) and recomputes the invariant curve. This process is repeated until the estimated error  $E(\varphi, \omega)$  is small enough.

#### IV.III Application to the EH3BPS

The previous technique can be easily applied to the EH3BPS. For instance, let  $\gamma(f)$ ,  $0 \leq f \leq T$  be a periodic orbit (of period  $T$ ) of this model for  $e = 0$  (think of any Lyapunov or Halo orbit). Now consider the effect of the stroboscopic map  $F$  defined before on this periodic orbit: for a given point of the periodic orbit,  $\gamma(f_0)$ , we have that  $F(\gamma(f_0)) = \gamma(f_0 + 2\pi)$ . This means that, under  $F$ , the periodic orbit becomes an invariant curve of rotation number  $\frac{4\pi^2}{T}$  (to obtain this value we have “scaled” the parametrization of the periodic orbit from  $[0, T]$  to  $[0, 2\pi]$ ). In this way we obtain an invariant curve (and its rotation number) of  $F$  for  $e = 0$ . Then, we can start a continuation method to increase the value of  $e$  from 0 to the actual value of the asteroid. Once the final value is reached, we can also continue the invariant curves w.r.t.  $\omega$  to produce the corresponding family of curves.

An extra technical difficulty that appears in these computations is the high instability of the region around  $SL_2$ . This implies that it is not practical to use the stroboscopic map  $F$  since the integration time ( $2\pi$ ) is quite long and the trajectories go far away from the neighbourhood of  $SL_2$  during this time. The standard tool to deal with this situation is the so-called parallel shooting.<sup>2</sup> Here, due to the high instability, we have used 100 sections for the parallel shooting.

#### IV.IV Results

We have computed invariant tori corresponding to the planar and vertical Lyapunov families, and the Halo orbits.

To represent these solutions, we will use the slice  $f = 0$ . In this way, the invariant tori are invariant curves that can be represented in the same way we have represented periodic orbits. On the other hand, to draw a single torus, we can take a mesh of points on the invariant curve and integrate each point till  $f = 2\pi$ . Note that the integrated trajectory lands on the invariant curve so that the set formed by the invariant curve plus these trajectories starting and ending on the curve (in different points) is the torus. A single or-

bit can also be visualized as an “spiraling” trajectory that touches the invariant curve each time  $f$  is a multiple of  $2\pi$ .

Figures 12 and 14 show the planar and vertical families of Lyapunov tori. They are similar to the families of periodic Lyapunov orbits seen before, and the dynamics can be summarized as the composition of two motions: the motion along the periodic Lyapunov orbit and a  $2\pi$  periodic motion given by the eccentricity. In Figures 13 and 15 we display a single torus from each of these families.

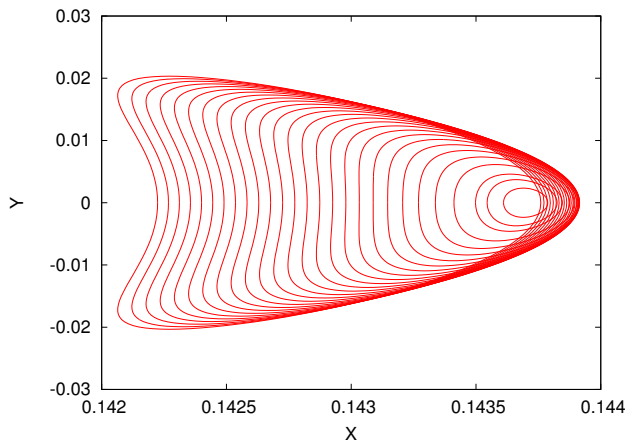


Fig. 12: Planar family of Lyapunov tori. Each closed curve is the  $((x, y)$  projection of the) slice of a tori with  $f = 0$ .

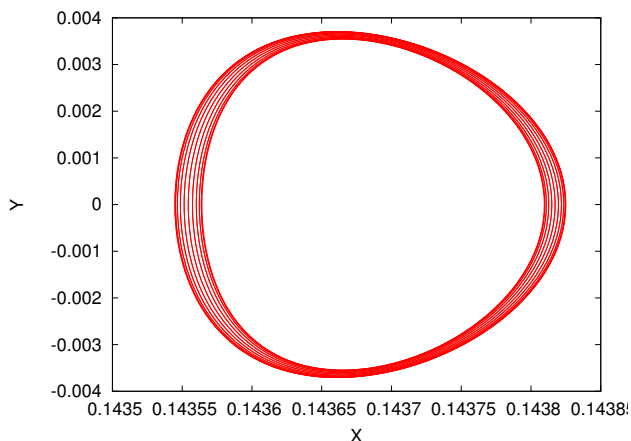


Fig. 13: A torus from the planar Lyapunov family.

Finally, Figure 16 shows a torus corresponding to a Halo orbit, as seen from the asteroid.

Finally, we recall that all these solutions are unstable. A detailed study of their stable/unstable manifold, and how to perform an efficient station keeping nearby is work in progress.

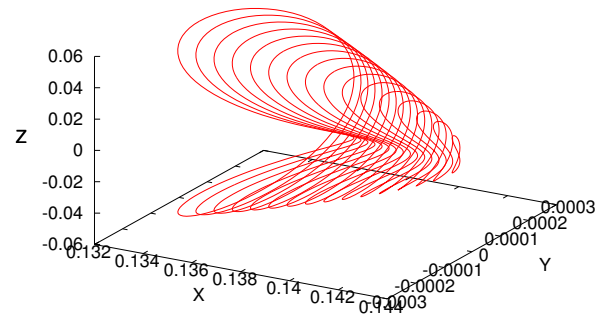


Fig. 14: Vertical family of Lyapunov tori. Each closed curve is the  $((x, y, z)$  projection of the) slice of a tori with  $f = 0$ .

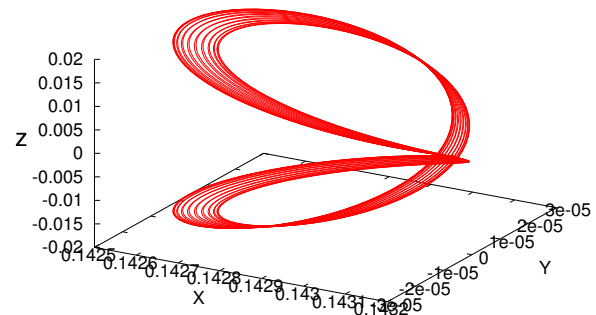


Fig. 15: A torus from the vertical Lyapunov family.

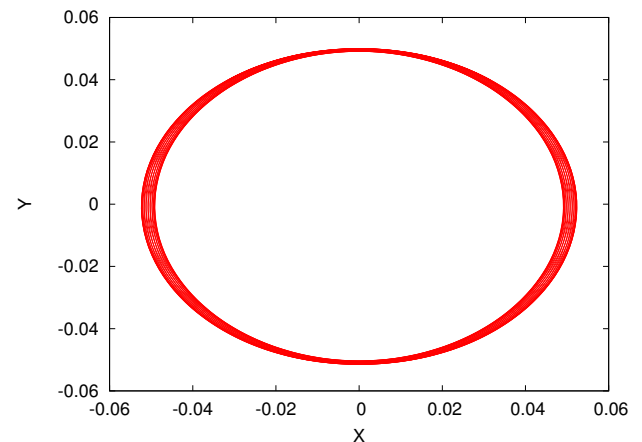


Fig. 16: Torus corresponding to a Halo orbit.

## V. CONCLUSIONS

In this paper we have done a preliminary study of the dynamics of a solar sail close to an asteroid. We have taken

as a model the Elliptic Hill three body problem, which accounts for the gravitational attraction of both Sun and asteroid, the effect of the eccentricity of the orbit of the asteroid, plus the SRP. As an example we have considered a small solar sail, with an area to mass ratio of  $0.025m^2/kg$ , orbiting near Vesta.

In section III. we show how the dynamics of the Circular Hill problem (the effect of the eccentricity  $e$  is neglected) is affected when we add the effect of the solar sail. We see how we can displace the position of the equilibrium points by changing the sail orientation. Moreover, we find different families of periodic orbits for different sail orientations.

In section IV. we show what happens when we add the effect of the eccentricity. The differential equations are now time dependent, which implies that the equilibrium points are replaced by periodic orbits, and most of the periodic orbits are replaced by quasi-periodic ones. We have computed some of these trajectories for  $e = 0.0882$  (Vesta's eccentricity). We can see that the families of planar and vertical orbits as well as Halo orbits persist when we add the effect of the eccentricity, although now they are no longer periodic but quasi-periodic.

In the near future, we plan to extend this work to the case of other asteroids. This means to study the case of other eccentricities and values of  $\bar{\beta}$ . We recall that as  $\bar{\beta}$  increases also does the instability of the orbits, and numerical challenges appear.

On the other hand, we have seen that all of these orbits are linearly unstable, hence an active control strategy must be used to remain close to them. Studies on the controllability of these objects are in progress.

## VI. Acknowledgement

This work has been supported by the MEC grant MTM2009-09723 and the CIRIT grant 2009 SGR 67.

## References

- [1] E. Castellà and À. Jorba. On the vertical families of two-dimensional tori near the triangular points of the Bicircular problem. *Celestial Mech.*, 76(1):35–54, 2000.
- [2] À. Jorba and E. Olmedo. On the computation of reducible invariant tori on a parallel computer. *SIAM J. Appl. Dyn. Syst.*, 8(4):1382–1404, 2009.
- [3] À. Jorba and J. Villanueva. On the persistence of lower dimensional invariant tori under quasi-periodic perturbations. *J. Nonlinear Sci.*, 7:427–473, 1997.
- [4] Y. Katherine and B. Villac. Periodic orbits families in the hill's three-body problem with solar radiation pressure. In *Advances in the Astronautical Sciences Series*, volume 136, San Diego, Colifornia, 2010.
- [5] K.R. Meyer and G.R. Hall. *Introduction to Hamiltonian Dynamical Systems and the N-Body Problem*. Springer, New York, 1992.
- [6] E. Morrow, D. Scheeres, and D. Lubin. Solar sail orbit operations at asteroids. *Journal of Spacecraft and Rockets*, 38(2):279–286, March-April 2001.
- [7] E. Morrow, D. Scheeres, and D. Lubin. Solar sail orbit operations at asteroids: Exploring the coupled effect of an imperfectly reflecting sail and a nonspherical asteroid. In *AIAA/AAS Astrodynamics Specialist Conference and Exhibit*, Monterey, California, 2002.
- [8] D.J. Scheeres. Orbital mechanics about small bodies. *Acta Astronautica*, 72(0):1 – 14, 2012.
- [9] B. Villac, G. Ribalta, A. Farrés, À. Jorba, and J-M. Mondelo. Using solar arrays for orbital control near small bodies. trade-offs characterization. In *AIAA/AAS Astrodynamics Specialist Conference*, 2012.